

<sup>1</sup> Parallel ghost imaging with extra large field of view and  
<sup>2</sup> high pixel resolution

<sup>3</sup> Nixi Zhao,<sup>1,2,3</sup> Jie Tang,<sup>1,2,3</sup> Changzhe Zhao,<sup>1,2,3</sup> Jianwen Wu,<sup>1,2,3</sup> Han  
<sup>4</sup> Guo,<sup>2</sup> Haipeng Zhang,<sup>2,\*</sup> and TiQiao Xiao<sup>1,2,3,\*</sup>

<sup>5</sup> *<sup>1</sup>Shanghai Institute of Applied Physics, Chinese Academy of Sciences, Shanghai 201800, People's  
6 Republic of China*

<sup>7</sup> *<sup>2</sup>Shanghai Synchrotron Radiation Facility/Zhangjiang Lab, Shanghai Advanced Research Institute,  
8 Chinese Academy of Sciences, Shanghai 201204, People's Republic of China*

<sup>9</sup> *<sup>3</sup>University of Chinese Academy of Sciences, Beijing 100049, People's Republic of China*

<sup>10</sup> *\*tqxiao@sari.ac.cn*

<sup>11</sup> *\*zhanghp@sari.ac.cn*

<sup>12</sup> Abstract: Ghost imaging (GI) facilitates image acquisition under low-light conditions through  
<sup>13</sup> single-pixel measurements, thus holding tremendous potential across various fields such as biomedical  
<sup>14</sup> imaging, remote sensing, defense and military applications, and 3D imaging. However, in  
<sup>15</sup> order to reconstruct high-resolution images, GI typically requires a large number of single-pixel  
<sup>16</sup> measurements, which imposes practical limitations on its application. Parallel ghost imaging  
<sup>17</sup> addresses this issue by utilizing each pixel of a position-sensitive detector as a bucket detector  
<sup>18</sup> to simultaneously perform tens of thousands of ghost imaging measurements in parallel. In this  
<sup>19</sup> work, we explore the non-local characteristics of ghost imaging in depth, and by constructing  
<sup>20</sup> a large speckle space, we achieve a reconstruction result in parallel ghost imaging where the  
<sup>21</sup> field of view surpasses the limitations of the reference arm detector. Using a computational  
<sup>22</sup> ghost imaging framework, after pre-recording the speckle patterns, we are able to complete  
<sup>23</sup> ghost imaging at a speed of 6 minutes per sample, with image dimensions of  $14000 \times 10000$   
<sup>24</sup> pixels ( $4.55\text{mm} \times 3.25\text{mm}$ , millimeter-scale field of view) and a pixel resolution of  $0.325\text{ }\mu\text{m}$   
<sup>25</sup> (sub-micron pixel resolution). We present this framework to enhance efficiency, extend reso-  
<sup>26</sup> lution, and dramatically expand the field of view, with the aim of providing a solution for the  
<sup>27</sup> practical implementation of ghost imaging. From a commercialization perspective, the ultimate  
<sup>28</sup> form of this work may be achieved with just a very inexpensive detector featuring a large field  
<sup>29</sup> of view and large pixel size, alongside a high-resolution detector with only a single pixel. This  
<sup>30</sup> represents a framework that is completely opposite to conventional ghost imaging.

<sup>31</sup> 1. Introduction

<sup>32</sup> Light emitted by an object passes through an optical system to form an inverted virtual image,  
<sup>33</sup> as seen in human vision, cameras, and lenses, all of which fall under the category of classical  
<sup>34</sup> imaging. These systems generally consist of three key components: the light source, the object,  
<sup>35</sup> and the optical system. In contrast, ghost imaging (GI), a novel imaging technique, employs  
<sup>36</sup> a non-local imaging approach that enables the separation of detection and imaging. In this  
<sup>37</sup> work, we further explore the non-local characteristics of ghost imaging, expanding the separation  
<sup>38</sup> between the detector size and the imaging field of view.

<sup>39</sup> Ghost imaging originates from the HBT experiment [1, 2]. In 1988, Klyshko [3] theoreti-  
<sup>40</sup> cally proposed a ghost imaging scheme using entangled photon pairs. In 1994, Ribeiro et al. [4]  
<sup>41</sup> discovered ghost interference phenomena through entangled photon pairs. In 1995, Pittman et  
<sup>42</sup> al. [5] experimentally realized ghost imaging using entangled photon pairs. In 2002, Bennink  
<sup>43</sup> et al. [6] demonstrated ghost imaging with classical light sources, proving that entangled light  
<sup>44</sup> sources are not a necessary condition for ghost imaging. Furthermore, GI has shown feasibility  
<sup>45</sup> in various fields, including atomic [7], electronic [8], neutron [9,10], and X-ray imaging [11–15].  
<sup>46</sup> In 2008, Shapiro [16] theoretically proposed the concept of computational ghost imaging, mak-

47 ing single-path ghost imaging possible. In 2009, Bromberg et al. [17] experimentally realized  
48 computational ghost imaging. That same year, Katz et al. [18] combined the technique of com-  
49 pressed sensing from the field of image processing with computational ghost imaging, signifi-  
50 cantly reducing the number of measurements needed for acquisition. This breakthrough enabled  
51 the reduction of radiation doses in X-ray-based ghost imaging.

52 However, if GI wants to reconstruct high-resolution images, it usually requires a large number  
53 of single pixel measurements, which poses difficulties for its practical application. Based on  
54 this, the concept of Parallel Ghost Imaging (PGI) was proposed by Kingston et al. to solve this  
55 problem [9]. This method treats each pixel of a position sensitive detector as an independent  
56 bucket detector and performs tens of thousands of ghost imaging simultaneously in parallel in  
57 one measurement. Kingston et al. and Zhang et al. respectively achieved PGI on neutron [9] and  
58 X-ray [19, 20]. However, the implementation of PGI through manually fitting bucket detector  
59 arrays only serves to validate the feasibility of the concept. It lacks the intrinsic characteristics  
60 of PGI, such as large field-of-view (FOV), enhanced resolution, and reduced dose. After a long  
61 time, we experimentally achieved parallel ghost imaging for the first time by using true magnifi-  
62 cation between the object arm and the reference arm. Improved the imaging resolution of PGI  
63 and significantly improved experimental efficiency.

64 In this work, we further expanded the imaging field while maintaining the pixel resolution of  
65 PGI ( $0.325\mu\text{m}$ ) and experimental efficiency (6 minutes per sample), surpassing the physical limit  
66 of the reference arm field of view. By collecting multiple sets of reference arm speckle patterns  
67 and seamlessly stitching them together to construct a extra large speckle space, we ultimately  
68 achieved ghost imaging with an image size of  $14000 \times 10000$  pixels. After completing the  
69 pre recording of the reference arm, we completed the measurement of the sample signal in just  
70 6 minutes, achieving imaging with millimeter level field of view and sub micron level pixel  
71 resolution, and the image results have good quality, which is unprecedented in the field of ghost  
72 imaging. We have achieved parallel ghost imaging with extra large field of view, high pixel  
73 resolution, and high experimental efficiency. We believe this framework will pave the way for  
74 the practical application of ghost imaging. If we infer the development direction of parallel ghost  
75 imaging from a commercial perspective, the most likely approach is to install a very inexpensive  
76 position sensitive detector with large field of view and pixel size on the object arm as a bucket  
77 detector array; High resolution detectors are expensive, so we only need a one pixel detector to  
78 move and record and stitch together a huge speckle space. We were surprised to find that this  
79 would be a completely opposite framework to conventional ghost imaging.

## 80 2. Experimental methods and results

81 The imaging process of ghost imaging is as follows: the light emitted by the light source is  
82 divided into two identical beams in the object arm and the reference arm after passing through  
83 the modulator and beam splitter. The sample is placed on the object arm and a bucket detector  
84 without spatial resolution, i.e. a single pixel detector, is used to receive the object arm signal.  
85 No object is placed in the reference arm, and the light is directly directed onto the detector with  
86 spatial resolution. The object arm has an object but no spatial resolution, and the reference  
87 arm has spatial resolution but no object. Neither of them can obtain object information alone,  
88 but by correlating the two, object images can be obtained. Based on this, ghost imaging, also  
89 known as correlation imaging, is a non local imaging method that decouples detection from  
90 imaging. Ghost imaging is meaningful in the field of X-rays because of its non local nature. We  
91 can transfer the high ionizing radiation dose required for high-resolution and large field of view  
92 imaging of objects to the air of the reference arm to bear, thereby achieving low-dose imaging.  
93 In this work, we further explore the non-local properties of ghost imaging, decoupling the size of  
94 the reference arm detector from the imaging field of view, thus achieving parallel ghost imaging  
95 with both extra large FOV and high resolution.

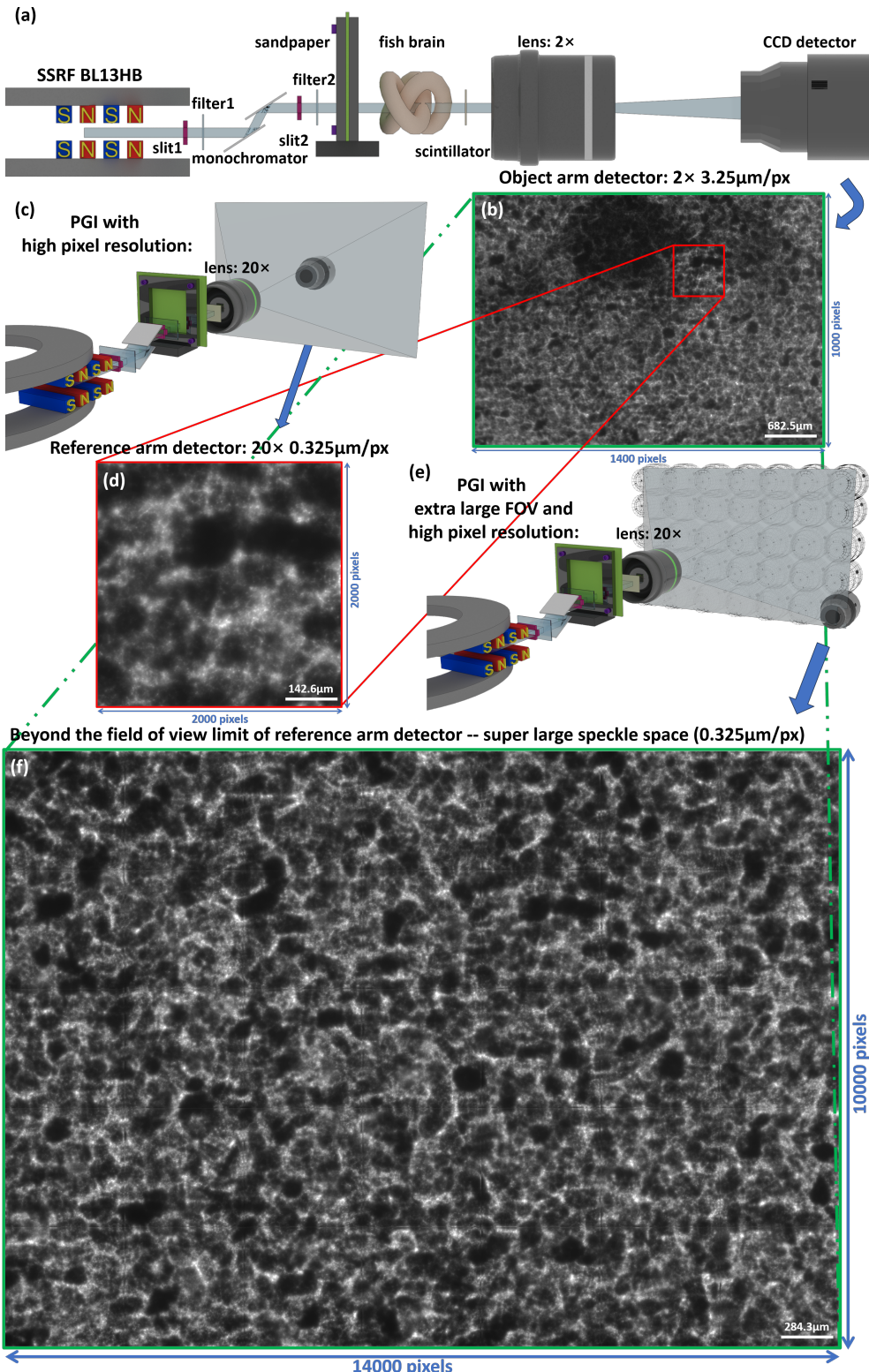


Fig. 1. (a)Schematic diagram of the object arm in the parallel ghost imaging experiment. (b)The signal coupling between the object and speckle collected from (a). (c)Schematic diagram of the reference arm in high-resolution parallel ghost imaging experiment. (d)The high-resolution speckle patterns collected from (b). (e)Schematic diagram of the reference arm in extra-large FOV and high-resolution parallel ghost imaging experiment. (f)The extra-large field and high-resolution speckle patterns collected from (e)

96        The ghost imaging system is a linear system, and the model for collecting data can be expressed  
 97        as:

$$Ax = b \quad (1)$$

98        where  $A \in R^{m \times n}$  is the matrix formed by the speckle patterns, which are vectorized. In the ex-  
 99        periment,  $m$  measurements are made, each with a speckle pattern containing  $n$  pixels.  $x \in R^{n \times 1}$   
 100       is the target image we seek to reconstruct, also expressed as a vector.  $b \in R^{m \times 1}$  is the sequence  
 101       of single-pixel signals collected by the bucket detector. All ghost imaging algorithms aim to  
 102       extract as much information about the object  $x$  as possible from the speckle patterns  $A$  and the  
 103       bucket signals  $b$ . In parallel ghost imaging, each pixel of the position-sensitive detector is treated  
 104       as a bucket detector, allowing tens of thousands of single-pixel ghost imaging measurements to  
 105       be performed simultaneously.

106       PGI employs a Total Variation Augmented Lagrangian Alternating Direction Method (TVAL3)  
 107       based on compressed sensing [21], which is a method for solving the unknown image iteratively  
 108       from the underdetermined system of linear equations. TVAL3 [22] introduces prior knowledge  
 109       of the signal to significantly reduce the number of measurements and lower the dose. The nat-  
 110       ural image prior used in TVAL3 is Total Variation (TV) regularization, which is based on the  
 111       statistical sparsity of image gradients in natural images. TVAL3 can be simplified as:

$$\begin{aligned} & \text{Min} ||c||_{l_0} \\ & \text{s.t. } Dx = c; \\ & Ax = b \end{aligned} \quad (2)$$

112       where  $Ax = b$  is the measurement model of ghost imaging,  $D$  is the transformation matrix that  
 113       converts the object image  $x$  to  $c$ , and the  $l_0$ -norm computes the number of non-zero elements in  $c$ .  
 114       The goal is to minimize this measure to find a sparse solution. Since the  $l_0$ -norm is a non-convex  
 115       function and difficult to solve directly, the  $l_1$ -norm is often used as an approximation. TVAL3  
 116       requires far fewer measurements than other methods to achieve comparable reconstruction qual-  
 117       ity, and it converges faster than most linear iterative methods. It is currently one of the most  
 118       powerful ghost imaging algorithms and has been validated through numerous experiments.

119       We have established an experimental platform at the X-ray imaging and biomedical application  
 120       beamline BL13HB [23] of the Shanghai Synchrotron Radiation Facility (SSRF) to implement  
 121       parallel ghost imaging within the computational ghost imaging framework. The modulator is a  
 122       7-layer, 200-mesh sandpaper, and the speckle patterns have a significant impact on the quality of  
 123       ghost imaging, which will be discussed and analyzed later. The photon energy used in the exper-  
 124       iment is 15 keV. The sample chosen for this experiment is a fish brain with high complexity and  
 125       low absorption contrast, aiming to challenge the ultimate capabilities of parallel ghost imaging.  
 126       The imaging system consists of a 100  $\mu\text{m}$  thick scintillation crystal (LuAG:Ce), an optical con-  
 127       version microscope (Model: Optique Peter MICRX016), and an sCMOS detector (Hamamatsu  
 128       ORCA-Flash 4.0 C11440). The detector has an effective area of  $6.6 \times 6.6 \text{ mm}^2$ , pixel size of 6.5  
 129        $\mu\text{m}$ , and a resolution of  $2048 \times 2048$  pixels. The experimental setup for recording the object arm  
 130       is shown in Fig.1.(a). Different energy beams are emitted from a bending magnet and filtered  
 131       by a double-crystal monochromator to select a single energy. Slits are used before and after the  
 132       monochromator to adjust the beam shape, and filters are employed to block stray light.

133       Unlike conventional ghost imaging, where a completely different mask needs to be replaced  
 134       for each measurement, in parallel ghost imaging, the motor carrying the sandpaper only needs  
 135       to move by a distance slightly greater than the pixel size of the bucket detector array (3.25  $\mu\text{m}$ )  
 136       to replace the mask. This greatly enhances the experimental efficiency of ghost imaging, which  
 137       is a unique advantage of PGI. The movement path of the sandpaper for each measurement is  
 138       identical, ensuring that the speckle patterns recorded in the object arm correspond perfectly to  
 139       the multiple sets of speckle patterns recorded in the reference arm. The monochromatic light,

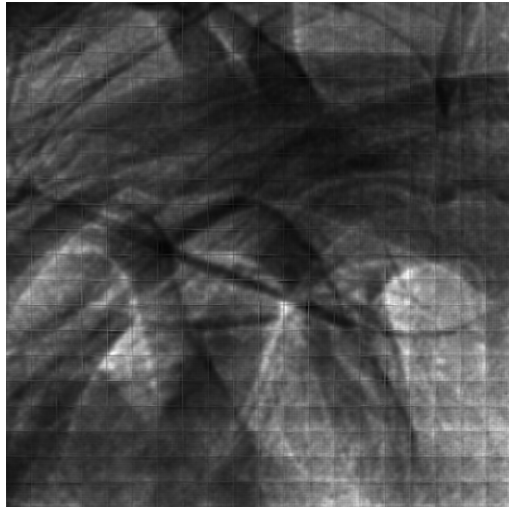


Fig. 2. High-resolution global ghost imaging reconstruction result: 400 measurements, 400% sampling rate, 0.325  $\mu\text{m}/\text{px}$  pixel resolution, 2000 $\times$ 2000 image size.

140 after passing through the scintillator, is converted to visible light. For recording the object arm, a  
 141 2 $\times$  magnification optical lens is used to capture the image of the sample coupled with the speckle  
 142 pattern, as shown in Fig.1.(b). By switching to a 20 $\times$  optical magnification lens, the effective  
 143 pixel size is reduced to 0.325  $\mu\text{m}$ , allowing the collection of speckle patterns with sub-micron-  
 144 level high resolution. The experimental setup for recording the high-resolution reference arm is  
 145 shown in Fig.1.(c), and the high-definition speckle image collected is shown in Fig.1.(d).

146 By aligning and reconstructing the 10 $\times$ 10 pixels from the reference arm with the correspond-  
 147 ing pixel positions in the object arm, high-resolution parallel ghost imaging can be achieved.  
 148 The reconstruction results in an image size of 2000 $\times$ 2000 pixels, with a pixel resolution of 0.325  
 149  $\mu\text{m}/\text{px}$ , as shown in Fig.2. One of the main challenges in this process is aligning the two sets of  
 150 data. We leave a margin of redundant pixels around the image edges and use the quality of the  
 151 reconstructed image as a criterion. The alignment is adjusted to minimize the error to less than  
 152 one reference arm pixel.

153 For the specific case of PGI, or the bucket detector array, we introduce the concept of Global  
 154 Ghost Imaging GGI . In this approach, all ghost imaging subsystems are uploaded to a central  
 155 processor where they are iteratively computed while sharing a global prior. This allows the it-  
 156 erative results to escape local optima and jointly find the global optimal solution. This method  
 157 significantly improves imaging quality and drastically reduces the number of measurements re-  
 158 quired for high-resolution ghost imaging, even down to single-digit measurements. More im-  
 159 portantly, it eliminates the discontinuities between the various ghost imaging subsystems. This  
 160 method has been thoroughly validated through simulations and experiments with manually fit-  
 161 ted bucket detector arrays. For parallel ghost imaging with true magnification, which is prone to  
 162 larger experimental errors, global ghost imaging improves reconstruction quality compared to  
 163 other methods. However, due to the need to load all subsystems into memory for simultaneous  
 164 computation, it places a considerable strain on computational resources. To address reconstruc-  
 165 tion efficiency, we perform the global ghost imaging reconstruction in blocks of 100 $\times$ 100 pixels  
 166 as a global domain and then stitch together the final result. Computational limitations currently  
 167 restrict the use of global ghost imaging for extra-large field-of-view ghost imaging. This neces-  
 168 sitates further modifications to the global imaging approach, which we aim to explore in future  
 169 work.

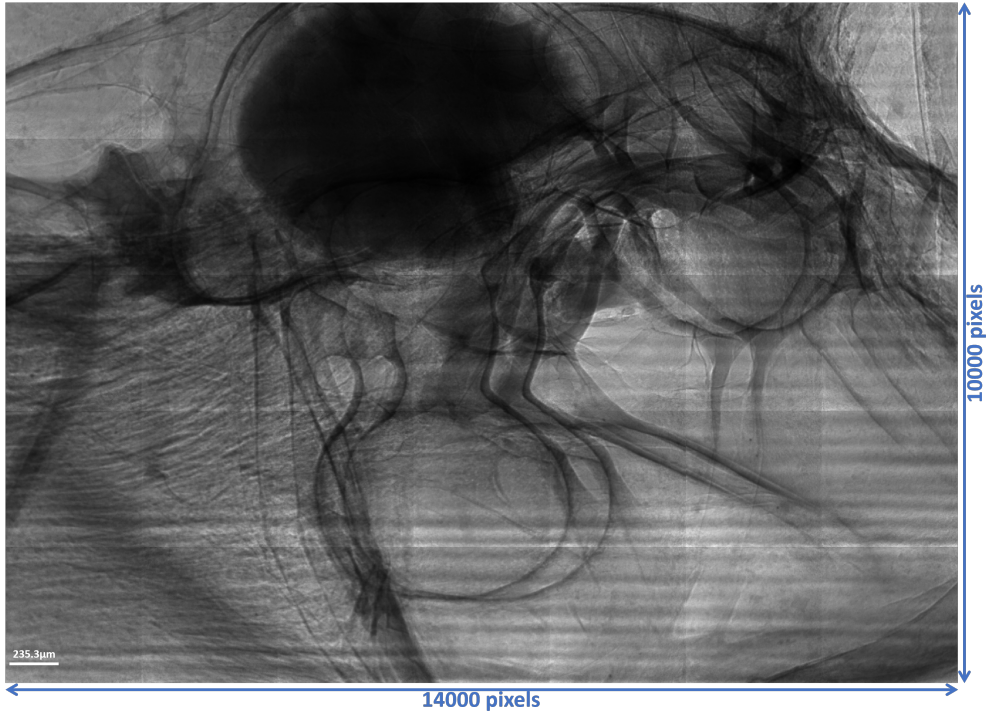


Fig. 3. Extra-large field of view and high-resolution parallel ghost imaging reconstruction result: 400 measurements, 400% sampling rate,  $0.325 \mu\text{m}/\text{px}$  pixel resolution,  $14000 \times 10000$  image size.

170 In fact, the potential of parallel ghost imaging has yet to be fully realized. The high-resolution  
 171 speckle patterns collected by the reference arm detector (Fig.1.(d)) actually only cover a small  
 172 portion of the object arm detector's field of view (Fig.1.(b)), as indicated by the red box. This  
 173 suggests that we can further exploit the non-local nature of ghost imaging. When pre-recording  
 174 the reference arm, instead of only capturing the set of speckle patterns with the magnification  
 175 lens switched (while keeping the detector fixed), we can record the entire large, high-resolution  
 176 speckle space corresponding to the object arm's field of view. This can be achieved by moving  
 177 the detector in a grouped manner, recording each set of speckle patterns and then stitching them  
 178 together. This approach means we will capture a total of  $7 \times 5$  groups of speckle patterns, which  
 179 takes about 5 hours, as shown in Fig.1.(f). The experimental diagram for the reference arm,  
 180 which enables both extra-large field-of-view and high-pixel resolution in parallel ghost imaging,  
 181 is shown in Fig.1.(e).

182 Finally, after completing the pre-recording of the reference arm, we successfully achieved  
 183 parallel ghost imaging with an experimental efficiency of 6 minutes per sample. The resulting  
 184 images had a size of  $14,000 \times 10,000$  pixels, a pixel resolution of  $0.325 \mu\text{m}$ , and good image  
 185 quality. A total of 400 measurements were made, with a sampling rate of 400%, and the recon-  
 186 struction results are shown in Fig.3.

187 It is important to note that the substantial expansion of the field of view is an enhancement  
 188 with no negative side effects. Due to the non-local nature of ghost imaging, the ionizing radi-  
 189 ation dose absorbed by the sample in the object arm has not increased at all. Fig.2 and Fig.3,  
 190 which use the same set of speckle patterns from the object arm, provide strong evidence for this  
 191 assertion. Thanks to the computational ghost imaging framework, the lengthy reference arm ac-

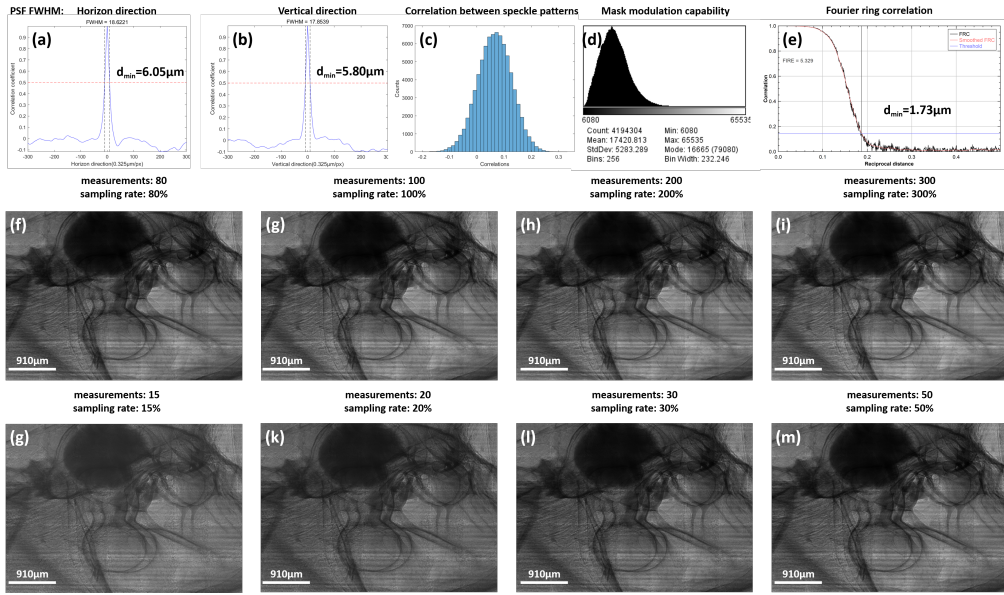


Fig. 4. Analysis of randomly modulated speckle patterns: (a) Point spread function (PSF) of the speckle in the horizontal direction. (b) Point spread function of the speckle in the vertical direction. (c) Statistical histogram of the correlation between the speckle patterns. (d) Histogram of the modulation capability of the mask. (e) Fourier ring correlation analysis of the mask resolution. Parallel ghost imaging reconstruction results with sampling rates of (i)300%, (h)200%, (g)100%, (f)80%, (m)50%, (l)30%, (k)20%, and (g)15%.

192 quisition only needs to be performed once. This means that the same expensive high-resolution  
 193 detector can be used to pre-record data for dozens of cheap, large-field-of-view, and large-pixel  
 194 detectors. Parallel ghost imaging shows great potential for achieving extra-large field-of-view  
 195 and super-resolution imaging at a low cost. In fact, it can significantly reduce the X-ray dose,  
 196 and we will continue to explore this in future work.

197 3. Discussion on speckle patterns, sampling rate, and reconstruction of extra-large  
 198 speckle space

199 Speckle patterns play a decisive role in the reconstruction quality of ghost imaging, as the resolu-  
 200 tion of the reconstructed image cannot be finer than the smallest effective feature of the speckle  
 201 patterns. In general, smaller pixels in the reference arm allow the detector to capture higher-  
 202 density mask information, which leads to better image quality. Larger pixels in the object arm  
 203 enable the detector to capture encoded object information more quickly, which results in a lower  
 204 radiation dose. The effective aperture of 200-mesh sandpaper is approximately 75  $\mu\text{m}$ , which  
 205 cannot describe the smallest feature of the mask. Irregular particle edges, sharp density gradi-  
 206 ents within the particles, and the stacking of seven layers of sandpaper all contribute to making  
 207 the minimum effective feature far smaller than the particle width. The mask's modulation capa-  
 208 bility for X-rays is shown in Fig.4.(d). The point spread function (PSF), as the autocovariance  
 209 of the mask pattern, sets the soft upper limit for the resolution of the final ghost imaging results.  
 210 However, at high sampling rates, the PSF may be surpassed. The full width at half maximum  
 211 (FWHM) of the PSF in both the horizontal and vertical directions is shown in Fig.4.(a) and (b).  
 212 The Fourier ring correlation (FRC), another spatial resolution criterion generated by the speckle

213 pattern, serves as the hard upper limit for GI resolution. The FRC of PGI is  $1.73\text{ }\mu\text{m}$ , smaller than  
214 the  $3.25\text{ }\mu\text{m}$  pixel size of the object arm detector, thus satisfying the super-resolution condition  
215 of ghost imaging, as shown in Fig.4.(e). These three characteristic length scales are interrelated  
216 but distinct. The reconstruction quality is also influenced by the degree of correlation between  
217 speckle patterns. If one speckle can be linearly combined with others, it represents ineffective  
218 sampling. The statistical histogram of the correlation levels between any two speckles (combi-  
219 nation of  $C_{400}^2$ ) is shown in Fig.4.(c), which implies that random speckles can be approximated  
220 as mutually orthogonal.

221 As mentioned earlier, ghost imaging, when combined with compressed sensing, can signifi-  
222 cantly reduce the number of measurements required to achieve high-quality reconstructions. A  
223 lower sampling rate means higher experimental efficiency and lower radiation dose. The recon-  
224 struction results at different sampling rates, from high to low, are shown in Fig.4.(f-m). With  
225 low sampling rates and few measurements, parallel ghost imaging with extra-large field-of-view  
226 and high-pixel resolution still performs well.

227 In the experiment, various factors such as X-ray energy, block size, registration between the  
228 reference and object arms, lens distortion, experimental errors, and sample complexity all af-  
229 fected the final image quality. Among these, the registration issue was the most critical. Par-  
230 allel ghost imaging still has considerable room for improvement in terms of resolution in the  
231 reconstruction results. If these issues can be addressed, the reconstruction could reveal many  
232 fundamental details of the sample that are currently invisible, transforming the "ghost" images  
233 into more informative representations. Based on this, there is still a long road ahead for further  
234 development.

235 Finally, we discuss several methods for reconstructing extra-large speckle place. In fact, due  
236 to the sub-micron precision required, reconstructing an extra-large speckle space is also a signif-  
237 icant experimental challenge. We proposed three approaches to achieve this:

238 (1) The first method is the most efficient: directly move the sandpaper to seamlessly stitch  
239 together a complete sandpaper plane, then simulate the collection by virtually moving a  $14,000$   
240  $\times 10,000$  pixel window within it. This approach requires only a few dozen sandpaper patterns to  
241 be captured and takes only a few seconds, theoretically making it feasible. However, in practical  
242 experiments, due to the presence of background stripes in the captured images, simulating the  
243 collection was not feasible. Moreover, in such high-precision experiments, we found that tiny  
244 gaps between the seven layers of the mask, as well as slight tilting of the entire sandpaper in  
245 the U/V directions, caused the speckles to change in size as they moved, with nearby speckles  
246 appearing larger and distant ones smaller. This approach requires high-precision alignment of  
247 the mask-carrying stage, which is difficult to achieve in time-constrained synchrotron radiation  
248 experiments.

249 (2) The second method is to move the sandpaper to construct a large mask space. For each  
250 measurement, 400 images are captured, repeated for 35 sets. This method is time-consuming  
251 but feasible. However, the precision of the five-axis stage carrying the sandpaper cannot be  
252 guaranteed, making it difficult to manually register the speckles in both the reference and object  
253 arms. For this reason, we used the third method in the experiment.

254 (3) To ensure absolute precision, we realized that the entire optical platform, OT2, which holds  
255 two detectors, had been perfectly calibrated. This ensures that the  $6.5\text{ }\mu\text{m}$  and  $9\text{ }\mu\text{m}$  detectors,  
256 located at a significant distance from each other, can switch without error. The movement of the  
257 sandpaper can be equivalently represented by the reverse relative movement of the detectors, and  
258 the precision of the detectors' movement is the highest. Our calculations show that even on the  
259 scale of over ten thousand pixels, the skew is only a few pixels, which improves registration and  
260 reconstruction results. Therefore, we chose to construct the extra-large speckle space by moving  
261 the detectors.

262 In fact, methods (2) and (3) are equivalent in principle, both being highly time-consuming.

263 We will continue to refine and improve method (1) in hopes of compressing the several hours of  
264 reference arm data collection into just a few minutes.

265 4. Conclusion

266 In conclusion, after achieving high spatial resolution and high imaging efficiency in parallel  
267 ghost imaging, we further dramatically expanded the imaging result's field of view by construct-  
268 ing a vast speckle space. This major advancement came at no unexpected cost, meaning that  
269 the experiment can still collect data at a rate of 6 minutes per sample, without any increase in  
270 radiation dose. Using the complex fish brain as a sample, we achieved ghost imaging with an  
271 image size of  $14,000 \times 10,000$  pixels ( $4.55\text{ mm} \times 3.25\text{ mm}$ , millimeter-scale field of view) and a  
272 pixel resolution of  $0.325\text{ }\mu\text{m}$  (sub-micron pixel resolution). We present this framework that en-  
273 ables ghost imaging with an extra-large field of view, ultra-high efficiency, and ultra-high pixel  
274 resolution, with the aim of providing a solution for the practical application of ghost imaging.  
275 This method can be implemented with simple experimental equipment and is feasible for X-rays,  
276 neutrons, and visible light, offering broad prospects for future applications.

277 **Funding.** The National Key Research and Development Program of China (Grant Nos. 2022YFA1603601,  
278 2021YFF0601203, 2021YFA1600703), the Young Scientists Fund of the National Natural Science Foun-  
279 dation of China (Grant No.12205361)

280 **Acknowledgment.** The authors thank WenJie Hao, Kang Du, Zenghao Song, JunXiong Fang, YanLing  
281 Xue, Ke Li and FeiXiang Wang for their kind help and fruitful discussion on experiments and data process-  
282 ing.

283 **Disclosures.** The authors declare no conflicts of interest.

284 **Data Availability Statement.** Data underlying the results presented in this paper are not publicly available  
285 at this time but may be obtained from the authors upon reasonable request.

286 References

- 287 1. R. Hanbury Brown and R. Q. Twiss, "A test of a new type of stellar interferometer on sirius," in *A Source Book in*  
288 *Astronomy and Astrophysics, 1900–1975*, (Harvard University Press, 1979), pp. 8–12.
- 289 2. R. H. Brown and R. Q. Twiss, "Correlation between photons in two coherent beams of light," *Nature* **177**, 27–29  
290 (1956).
- 291 3. D. Klyshko, "Two-photon light: influence of filtration and a new possible epr experiment," *Phys. Lett. A* **128**, 133–  
292 137 (1988).
- 293 4. P. S. Ribeiro, S. Pádua, J. M. Da Silva, and G. Barbosa, "Controlling the degree of visibility of young's fringes with  
294 photon coincidence measurements," *Phys. Rev. A* **49**, 4176 (1994).
- 295 5. T. B. Pittman, Y. Shih, D. Strekalov, and A. V. Sergienko, "Optical imaging by means of two-photon quantum  
296 entanglement," *Phys. Rev. A* **52**, R3429 (1995).
- 297 6. R. S. Bennink, S. J. Bentley, and R. W. Boyd, "“two-photon” coincidence imaging with a classical source," *Phys.*  
298 *review letters* **89**, 113601 (2002).
- 299 7. R. I. Khakimov, B. Henson, D. Shin, *et al.*, "Ghost imaging with atoms," *Nature* **540**, 100–103 (2016).
- 300 8. S. Li, F. Cropp, K. Kabra, *et al.*, "Electron ghost imaging," *Phys. review letters* **121**, 114801 (2018).
- 301 9. A. M. Kingston, G. R. Myers, D. Pelliccia, *et al.*, "Neutron ghost imaging," *Phys. Rev. A* **101**, 053844 (2020).
- 302 10. Y.-H. He, Y.-Y. Huang, Z.-R. Zeng, *et al.*, "Single-pixel imaging with neutrons," *Sci. Bull.* **66**, 133–138 (2021).
- 303 11. H. Yu, R. Lu, S. Han, *et al.*, "Fourier-transform ghost imaging with hard x rays," *Phys. review letters* **117**, 113901  
304 (2016).
- 305 12. D. Pelliccia, A. Rack, M. Scheel, *et al.*, "Experimental x-ray ghost imaging," *Phys. review letters* **117**, 113902  
306 (2016).
- 307 13. A. Schori and S. Shwartz, "X-ray ghost imaging with a laboratory source," *Opt. express* **25**, 14822–14828 (2017).
- 308 14. D. Pelliccia, M. P. Olbinado, A. Rack, *et al.*, "Towards a practical implementation of x-ray ghost imaging with  
309 synchrotron light," *IUCrJ* **5**, 428–438 (2018).
- 310 15. A. Schori, D. Borodin, K. Tamasaku, and S. Shwartz, "Ghost imaging with paired x-ray photons," *Phys. Rev. A* **97**,  
311 063804 (2018).
- 312 16. J. H. Shapiro, "Computational ghost imaging," *Phys. Rev. A—Atomic, Mol. Opt. Phys.* **78**, 061802 (2008).
- 313 17. Y. Bromberg, O. Katz, and Y. Silberberg, "Ghost imaging with a single detector," *Phys. Rev. A—Atomic, Mol. Opt.*  
314 *Phys.* **79**, 053840 (2009).
- 315 18. O. Katz, Y. Bromberg, and Y. Silberberg, "Compressive ghost imaging," *Appl. Phys. Lett.* **95** (2009).

- 316 19. H. Zhang, K. Li, F. Wang, *et al.*, “Megapixel x-ray ghost imaging with a binned detector in the object arm,” Chin.  
317 Opt. Lett. **20**, 033401 (2022).
- 318 20. C.-Z. Zhao, H.-P. Zhang, J. Tang, *et al.*, “X-ray ghost imaging with a specially developed beam splitter,” Synchrotron  
319 Radiat. **31** (2024).
- 320 21. D. L. Donoho, “Compressed sensing,” IEEE Trans. on information theory **52**, 1289–1306 (2006).
- 321 22. C. Li, W. Yin, H. Jiang, and Y. Zhang, “An efficient augmented lagrangian method with applications to total variation  
322 minimization,” Comput. Optim. Appl. **56**, 507–530 (2013).
- 323 23. J.-F. Ji, H. Guo, Y.-L. Xue, *et al.*, “The new x-ray imaging and biomedical application beamline b113hb at ssrf,”  
324 Nucl. Sci. Tech. **34**, 197 (2023).